Hindawi

Retraction

Retracted: The Key Technology of Oblique Photogrammetry of Assembled Buildings by UAV

Advances in Multimedia

This article has been retracted by Hindawi following an investigation undertaken by the publisher [1]. This investigation has uncovered evidence of one or more of the following indicators of systematic manipulation of the publication process:

(1) Discrepancies in scope
(2) Discrepancies in the description of the research reported
(3) Discrepancies between the availability of data and the research described
(4) Inappropriate citations
(5) Incoherent, meaningless and/or irrelevant content included in the article
(6) Peer-review manipulation

The presence of these indicators undermines our confidence in the integrity of the article's content and we cannot, therefore, vouch for its reliability. Please note that this notice is intended solely to alert readers that the content of this article is unreliable. We have not investigated whether authors were aware of or involved in the systematic manipulation of the publication process.

Wiley and Hindawi regrets that the usual quality checks did not identify these issues before publication and have since put additional measures in place to safeguard research integrity.

We wish to credit our own Research Integrity and Research Publishing teams and anonymous and named external researchers and research integrity experts for contributing to this investigation.

The corresponding author, as the representative of all authors, has been given the opportunity to register their agreement or disagreement to this retraction. We have kept a record of any response received.

References

[1] J. Yao, J. Na, R. Ma, and Y. Wang, "The Key Technology of Oblique Photogrammetry of Assembled Buildings by UAV," *Advances in Multimedia*, vol. 2022, Article ID 6267403, 12 pages, 2022.

Research Article

The Key Technology of Oblique Photogrammetry of Assembled Buildings by UAV

Jian Yao [ID],[1] Jiaming Na,[2] Rong Ma,[1] and Yuyan Wang[1]

[1]*Institute of Construction Engineering, Shanxi College of Applied Science and Technology, Taiyuan 030062, China*
[2]*College of Civil Engineering, Nanjing Forestry University, Nanjing 210037, China*

Correspondence should be addressed to Jian Yao; 2021000605@poers.edu.pl

In order to ensure the disaster control during infrastructure construction and operation, a method of tilt photogrammetry of prefabricated buildings using UAV is proposed. A comparative study of the key steps in the 3D construction process of building (structure) was carried out, and a set of 3D morphology construction method based on UAV tilt photogrammetry was proposed, and the key steps were optimized to realize automation and visualization in the process of model construction. The experimental results show that in the application case of a school district, the error of the three directions is distributed between -4 cm and 4 cm, accounting for 74%, and that between -2 cm and 2 cm, accounting for 37%; the root mean square error of the three directions was calculated to be 4.0 cm, 3.8 cm, and 2.8 cm, respectively. In an engineering application case, the error size of the three directions distributed between -4 cm and 4 cm accounted for 74%, and that between -2 cm and 2 cm accounted for 50%; the root mean square error of the three directions was calculated as 2.3 cm, 2.5 cm, and 3.3 cm, respectively. *Conclusion.* This method can not only obtain high-precision 3D models of urban complex and single buildings, but also meet the requirements of digital city construction for 3D model construction and obtain clear and high-precision digital land surface model.

1. Introduction

After more than half a century of development, UAV photogrammetry technology has made remarkable achievements. It is an important part of surveying and mapping engineering discipline, and its theory and operation methods are updated day by day. With the continuous progress of science and technology, especially the rapid development of computer technology, tilt photography technology has been gradually developed by leaps and bounds. Different from the common photogrammetry technology, the oblique photography technology uses the camera to take pictures of the side, top surface, surface, and other normal surfaces of the building and then automatically determine the texture information of the building from all kinds of images. This technology can extract the picture information of any direction and any place and can guarantee the consistency with the actual structure. Combined with 3D light and shadow information in the shooting space, a 3D solid model with better authenticity and higher three-dimensional sense can be constructed [1]. In addition, relying on the huge parallel computing advantages of computers, tilt photogrammetry technology can quickly and efficiently complete three-dimensional modeling, and its modeling efficiency is higher than that of manual modeling. With the development of society, the cost of manual mapping will only gradually increase. On the contrary, the cost of computer hardware and software will tend to be cost-effective, so photogrammetry technology will gradually replace manual surveying and mapping means. UAV is the most common photogrammetric platform carrier and workstation, with high efficiency, convenient, fast, and low cost of measurement advantages. At present, UAV photogrammetry technology has been rapidly promoted and achieved satisfactory results in engineering practice [2]. In general, UAVs include fixed wing UAVs, multirotor UAVs, and fixed wing VTOL UAVs. These three types of UAVs have some differences in power drive, working time, and image resolution. In terms of power, fixed-

wing UAV is driven by fuel, while multirotor UAV is driven by battery. In terms of working time, fixed-wing UAV can fly for a long time, so it has certain advantages in large area measurement [3]. Multirotor UAVs generally have short flight time and low flying altitude, which also enables them to obtain high-resolution ground images. And this type of UAV makes it easy to install a tilt camera and then carry out tilt photogrammetry work. At present, UAV tilt photogrammetry has been widely used in the investigation of rural premises with its advantages of high accuracy, low cost, and fast efficiency.

2. Literature Review

Image feature matching can be divided into two matching methods based on gray level and feature based according to the different matching unit information. In the image matching for city modeling, there are many phenomena such as shadow, gray discontinuity, and occlusion due to the dense buildings, so the matching results based on grayscale are generally unreliable. The matching effect based on grayscale is not good. Klanfar et al. proposed a matching method with affine invariance for tilted images [4]. In the aspect of aerial triangulation, there are three main methods of aerial triangulation, namely aerial belt net method, independent model method, and beam method. Among them, the beam method is the most rigorous method, and the large amount of calculation is its main shortcoming. However, with the continuous improvement of computer software and hardware, this method has become the mainstream space three method in the traditional photogrammetry field and has been widely used. In terms of Dense Image Matching (DIM), according to the number of images processed, it can be divided into dense matching based on stereo image pairs and dense matching based on multiview correspondence. The former uses stereo pair matching to generate parallax map and then fuses the matching results. The latter generally uses constraint relation to match between multiview photos and then uses region growth algorithm to diffuse to the periphery [5]. Semiglobal matching (SGM) proposed by Alipour-Sarabi et al. has achieved good matching efficiency and matching effect [6]. Sezer et al. proposed a reliable matching method for tilted images that is suitable for near-plane scenes and complex 3D scenes [7]. In terms of surface reconstruction based on point cloud, Voronoi diagram proposed by Franco, Y. evolved Delaunay triangulation network, which can generate irregular TIN network based on sample point data [8]. Chen et al. proposed the Poisson surface reconstruction method, which is widely used in surface reconstruction based on point cloud data generated by image at present [9].

Based on the comparative study of the key steps in the process of assembling building model, this essay proposes a set of real scene model construction method based on UAV tilt photogrammetry. The key steps are optimized to realize automation and visualization in the process of model construction [10]. The key steps of real scene model construction include camera calibration, data acquisition, image preprocessing, and model construction. The key steps are theoretically deduced, and the realization method and process of each key step are introduced.

3. The Research Methods

3.1. Principles and Characteristics of Oblique Photogrammetry

3.1.1. Principle of Tilt Photogrammetry. UAV tilt photogrammetry is a concept relative to the traditional vertical photogrammetry. It breaks the problem that the traditional aerial survey can only obtain the orthographic image of the ground. An aircraft carrying multiple sensors can obtain the image data of the same building from orthographic and up, down, and around five angles, respectively. The built-in GPS receiver and high-precision IMU were used to determine the external orientation elements of the camera exposure point and record the flight altitude and photo exposure time of UAV [11]. The geometric relation and texture characteristics of ground object terrain are analyzed from the image information, and 3D reconstruction is carried out to obtain a photogrammetric method that satisfies the accuracy of 3D real scene model. Aerial survey operation of UAV is to use unmanned aerial vehicle carrying image acquisition device to carry out image data acquisition from vertical direction and tilt direction. The collection of image data from the vertical direction is called vertical photography and is mainly used to produce photogrammetric 4D products; image data collected from the oblique direction is called oblique photography, which is mainly used to produce three-dimensional models, which are more realistic and three-dimensional.

3.1.2. Characteristics of Oblique Photogrammetry. With the continuous improvement and development of low-altitude photogrammetry technology, the use of UAV to carry out aerial survey work has become a new development trend of surveying and mapping. In photogrammetry, the traditional manned aircraft has the characteristics of large range of image data acquisition, high image quality, long flight time, and strong controllability. However, when carrying out the work of manned aircraft, it is greatly affected by weather conditions, so the safety of pilots is difficult to be guaranteed. Compared with manned aircraft, UAV is superior to manned aircraft in terms of maneuverability and flexibility in photogrammetry operations, ensuring the safety of operators and greatly reducing the cost of aircraft timber and image data processing. In the process of data collection, the flight altitude, flight speed, flight direction, overlap, and other parameters are recorded at the same time, and then the collected data are analyzed and sorted out. Context Capture (original smart3D) software is used for later data processing and 3D model reconstruction.

3.2. Camera Calibration. Figure 1 is the flow chart of UAV oblique photogrammetry-based real scene model construction method.

In this study, the planar template calibration method is adopted, that is, during the calibration process, the camera needs to take a series of images with specific patterns. These
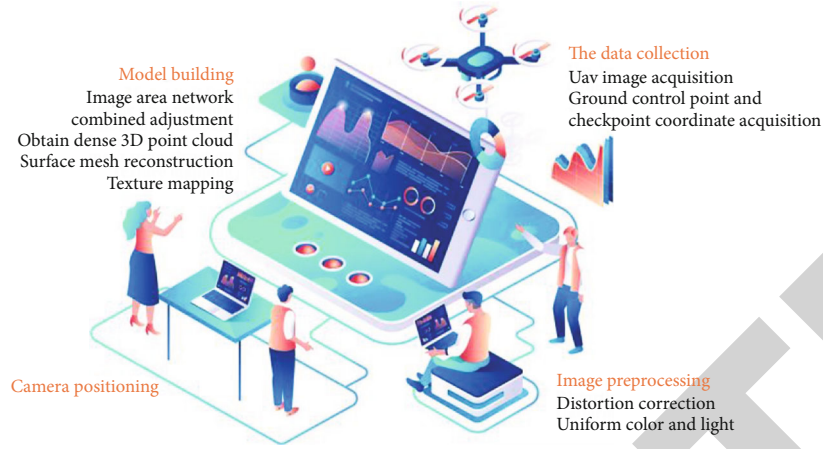
Figure 1: Flow chart of real model construction method.

special-pattern plates are called calibration targets. Through the camera photographing the flat plate with fixed spacing array, the geometric model of the camera can be obtained through calibration algorithm calculation, which provides parameters for distortion correction in image preprocessing. The first step is to obtain the initial values of internal parameters without considering the distortion. The second step is to perform nonlinear calculation under the condition that the obtained parameters are the initial values and iterate until the parameters converge.

3.2.1. Derivation of Formula

(1) Obtain the Initial Value of Camera Lens Parameters. If it is known that the coordinate of the feature point of the checkerboard on the calibration board is $\tilde{Q} = [X\,Y\,Z]^T$ in space, the coordinate of the corresponding point in the pixel coordinate system is $\tilde{q} = [u\,v]^T$ after imaging by the camera. $\tilde{Q}$ and $\tilde{q}$ can be expressed as $Q = [X\,Y\,Z\,1]^T$ and $q = [u\,v\,1]^T$ in homogeneous form, and their relationship is as follows:

$$sq = K[R\quad T]Q, \tag{1}$$

$$K = \begin{bmatrix} f_x & 0 & u_0 \\ 0 & f_y & v_0 \\ 0 & 0 & 1 \end{bmatrix}, \tag{2}$$

$$R = \begin{bmatrix} r_1 & r_2 & r_3 \\ r_4 & r_5 & r_6 \\ r_7 & r_8 & r_9 \end{bmatrix}, \tag{3}$$

$$T = \begin{bmatrix} t_1 \\ t_2 \\ t_3 \end{bmatrix}, \tag{4}$$

where s is the scale factor; K is the internal parameter matrix; and R and T are the rotation and translation matrices of the world coordinate system relative to the camera

coordinate system, respectively, which are called external parameter matrices.

It is assumed that the z-axis coordinate of the calibration plate in the world coordinate system is 0, that is, the world coordinate system is established on the calibration plate. Meanwhile, the rotation matrix R is expressed in the form of $R = [r_1\,r_2\,r_3]$, where r_1, r_2, and r_3 are column vectors of matrix R, respectively, and then Formula (1) can be expressed as

$$s\begin{bmatrix} u \\ v \\ 1 \end{bmatrix} = K[r_1\quad r_2\quad r_3\quad T]\begin{bmatrix} X \\ Y \\ 0 \\ 1 \end{bmatrix} = K[r_1\quad r_2\quad t]\begin{bmatrix} X \\ Y \\ 1 \end{bmatrix}. \tag{5}$$

Since =0, the coordinates of $\tilde{Q}$ and Q change to $\tilde{Q} = [X\,Y]^T$ and $Q = [X\,Y\,Z\,1]^T$, then the relation between point Q and its corresponding point q on the image can be expressed by such a homography matrix H as

$$sq = HQ, \tag{6}$$

wherein the following formula:

$$H = \mu K[r_1\quad r_2\quad t]. \tag{7}$$

H is a 3×3 homography matrix with only one scale factor difference. The homography matrix H is expressed as the form of row vector $H = \begin{bmatrix} \bar{h}_1^T & \bar{h}_2^T & \bar{h}_3^T \end{bmatrix}^T$. According to Equation (6), q and HQ have the same direction and differ in size by one scale factor, so the cross product of the two

is 0, namely

$$q \times HQ = \begin{bmatrix} u \\ v \\ 1 \end{bmatrix} \times \begin{bmatrix} \bar{h}_1^T Q \\ \bar{h}_2^T Q \\ \bar{h}^T Q \end{bmatrix} = \begin{bmatrix} 0 & -Q^T & vQ^T \\ Q^T & 0 & -uQ^T \\ -vQ^T & uQ^T & 0 \end{bmatrix} H. \tag{8}$$

The third line can be obtained by corresponding transformation of the first and second lines of Equation (8), so the equation can be transformed into the following equation:

$$q \times HQ = \begin{bmatrix} Q^T & 0 & -uQ^T \\ 0 & Q^T & -vQ^T \end{bmatrix} H, \tag{9}$$

where the matrix on the left is 2×9, which is represented by L. Then, if the corresponding points are given to a group of points n, the matrix on the left becomes 2n□. The matrix of 9 is

$$LH = 0. \tag{10}$$

Singular value decomposition (SVD) is performed on the matrix L, and the initial value of the homography matrix H is obtained.

(2) Calculation of Homography Matrix. The homography matrix H is written as $H = [h_1 h_2 h_3]$, wherein h_1, h_2, and h_3 are column vectors of matrix H, respectively, and then Equation (7) can be written as

$$[h_1 h_2 h_3] = \mu K [r_1 r_2 t]. \tag{11}$$

Namely, Formula (12) is as follows:

$$\left. \begin{array}{l} h_1 = \mu K r_1 \\ h_2 = \mu K r_2 \\ t = \mu K r_3 \end{array} \right\}, \tag{12}$$

where μ is the scale factor [12].

Given that the three column vectors of the rotation matrix are biorthogonal and are unit vectors, the following constraint conditions can be obtained as

$$\left. \begin{array}{l} r_1^T r_2 = 0 \\ r_1^T r_1 = r_2^T r_2 \end{array} \right\}. \tag{13}$$

By substituting Equation (12) into Equation (13), two constraint relations of internal parameters can be obtained as follows:

$$\left. \begin{array}{l} h_1^T K^{-T} K^{-1} h_2 = 0 \\ h_1^T K^{-T} K^{-1} h_1 = h_2^T K^{-T} K^{-1} h_2 \end{array} \right\}. \tag{14}$$

The coordinate of image coordinate q' obtained by projection of point Q is

$$q' = \frac{1}{\bar{h}_1 Q} \begin{bmatrix} \bar{h}_1 & Q \\ \bar{h}_2 & Q \end{bmatrix}. \tag{15}$$

The reprojection error is expressed as

$$\sum_i \left(q - q' \right)^T \Lambda_q^{-1} \left(q - q' \right), \tag{16}$$

where $\Lambda_q = \sigma^2 I$ is the covariance matrix and I is the identity matrix. The error between the actual pixel coordinate q in the image and the pixel coordinate q' calculated by using the parameters obtained is the reprojection error. Using Lenenberg-Marquardt method, the homography matrix H can be obtained by minimizing it.

(3) Solution of Parameters in Camera Lens. After obtaining the value of the homography matrix H, the internal parameter matrix of the camera can be obtained by this matrix.

Let the matrix $B = K^{-T} K^{-1}$ and substitute the expression of the internal parameter matrix K into the following equation:

$$B = \begin{bmatrix} B_{11} & B_{12} & B_{13} \\ B_{21} & B_{22} & B_{23} \\ B_{31} & B_{32} & B_{33} \end{bmatrix} = \begin{bmatrix} \dfrac{1}{f_x^2} & 0 & -\dfrac{u_0}{f_x^2} \\ 0 & \dfrac{1}{f_y^2} & -\dfrac{v_0}{f_y^2} \\ -\dfrac{u_0}{f_x^2} & -\dfrac{v_0}{f_y^2} & \dfrac{u_0}{f_x^2} + \dfrac{v_0}{f_y^2} + 1 \end{bmatrix}. \tag{17}$$

As can be seen from the expression of matrix B, it is actually a symmetric matrix B. Therefore, to define a six-dimensional vector, b containing the above elements is

$$b = \begin{bmatrix} B_{11} & B_{12} & B_{22} & B_{13} & B_{23} & B_{33} \end{bmatrix}. \tag{18}$$

Equation (14) can be expressed by $h_i^T B h_j$ as

$$h_i^T B h_j = v_{ij}^T b, \tag{19}$$

where $v_{ij} = [h_{i1}h_{j1} \; h_{i1}h_{j2} + h_{i2}h_{j1} \; h_{i2}h_{j2} \; h_{i3}h_{j1} + h_{i1}h_{j3} \; h_{i3}h_{j2} + h_{i2}h_{j3} \; h_{i3}h_{j3}]^T$. Then Formula (14) can be expressed as

$$\begin{bmatrix} v_{ij}^T \\ (v_{11} + v_{22})^T \end{bmatrix} b = 0. \tag{20}$$

Each picture corresponds to an equation (2.20), so when there are n pictures, there will be a set of equations. A matrix

of 2n□6 can be obtained by combining them in matrix form, which is expressed by V as the following equation:

$$V b = 0. \tag{21}$$

Similarly, when singular value decomposition is performed on V, the feature vector corresponding to its minimum eigenvalue is vector b, and the internal parameter of the camera can be calculated as follows:

$$
\left.
\begin{aligned}
v_0 &= \frac{B_{12} B_{13} - B_{11} B_{23}}{B_{11} B_{22} - B_{12}^2} \\
\mu &= \frac{B_{33} - \left[B_{13}^2 + v_0 (B_{12} B_{13} - B_{11} B_{23}) \right]}{B_{11}} \\
k_x &= \sqrt{\frac{\mu}{B_{11}}} \\
k_y &= \sqrt{\frac{\mu B_{11}}{B_{11} B_{22} - B_{12}^2}} \\
\mu_0 &= -\frac{B_{13} k_x^2}{\mu}
\end{aligned}
\right\}. \tag{22}
$$

(4) Solving the Parameters Outside the Camera Lens. When the internal parameters are known, the external parameters of the camera can be obtained according to Equation (7) as

$$
\left.
\begin{aligned}
\mu &= \frac{1}{K^{-1} h_1} = \frac{1}{K^{-1} h_2} \\
r_1 &= \mu K^{-1} h_1 \\
r_2 &= \mu K^{-1} h_2 \\
r_3 &= r_1 \times r_2 \\
t &= \mu K^{-1} h_3
\end{aligned}
\right\}. \tag{23}
$$

3.2.2. MATLAB Programming. According to the above formula, MATLAB is used to write programs to realize the automation and visualization of the camera calibration process. The specific implementation steps are as follows:

(1) Take 20 to 40 pictures with the calibration plate with the camera to be calibrated, and make sure that the relative position of the calibration plate and the camera does not repeat as much as possible; rename the image for later reading

(2) Run the main program of camera calibration and image preprocessing, and click "Camera Calibration" on the page to enter the camera calibration operation interface

(3) Click "Picture name", and the program reads all picture names under the picture path through dir function; at this time, "Basename Camera Calibration images:" will appear in the command window. Input the image prefix, such as "20180520." "Image for-

mat(Image type): ([]="r"="ras", "b" = "bmp", "t" = "tif", "p" = "pgm", "j" = "jpg", "g" = "jpeg", "m" = "ppm")," the type of the input image, for example, in jpg format, enter j

(4) Click "Read picture," and the program will read all pictures with "20180520" prefix and display the read picture and progress in the command window

(5) Click "to extract the corner [automatic]"; the program first identifies the four corner points of each calibration board and then through detectCheckerboardPoints. M functions all corners of the calibration board for automatic extraction [13]. During the process, the checkerboard number of the length and width of the calibration board and the size of the checkerboard can be input according to the prompts. The extracted corner coordinates and calibration progress of each photo will appear in the command window, and the calibration process will also be displayed in the form of plot through imshow function

(6) Click "Calibration," and the program calculates the corner coordinates of all photos extracted in step (5) to obtain the initial value of camera lens parameters and the optimized value after calibration. These include focal length, principal point, skew, tangential distortion, and pixel error

(7) Click "Save calibration result," and the program will save the calibration result in MAT file in the specified path, so that the parameters can be extracted by image distortion correction later

Click "Display external parameter" to get the relative position diagram of the camera and all picture calibration plates; click "Error Analysis" to get the error distribution of all the photo corners.

3.3. The Data Collection

3.3.1. UAV Image Acquisition. The UAV oblique photogrammetry technology is used to obtain multiple different angle images of the target area from different camera positions, including vertical shot images and oblique shot images.

The reasonable flight plan is determined according to the actual situation, including the design of flight altitude, route and speed, image shooting angle, camera parameters, camera frequency, heading and side image overlap degree, and other parameters. Reasonable flight planning can effectively reduce field workload and improve postprocessing efficiency and product accuracy [14]. Aerial photography records real-time flight altitude, latitude and longitude, geodetic height, attitude, and other information for subsequent analysis and sorting.

In this study, a certain UAV equipped with a certain camera was adopted with 20.8 million effective pixels and a focal length of 15 mm. The technical parameters are shown in Table 1. The UAV is equipped with stereo vision system

Image sensor	CMOS,4/3"
Camera pixels	20,800,000
Image resolution	4 : 3,5280X3956 6 : 9, 5280X2970
The camera focal length	15 mm
Angle of view (FOV)	72°
Maximum flying height	3000 m
Take-off weight	5.15 kg(big battery)/4.42 kg(small battery)
Maximum flat speed	18 m/s
Maximum flight time	32 min
Operating ambient temperature	From -20 °C to 45 °C

in front and below and infrared sensing system above, which can realize obstacle avoidance in front, below, and above. M210-rtk UAV is equipped with a real-time kinematic (RTK) module. It can receive Global Positioning System (GPS) and Beidou Satellite System (BDS) signals in real time and use ground reference stations for differential carrier phase correction. The UAV flight positioning information with plane accuracy of 1 cm and elevation accuracy of 2 cm can be obtained.

Currently, flight control apps commonly used in the market include DJI GO 4, DJI GS Pro, Altizure, and Pix4D-capture. In this study, DJI GS Pro flight control APP was used to preset the flight altitude, route, heading, image overlap degree, and shooting tilt Angle of each flight sorbet according to the ground situation to control the track and attitude of UAV, so as to ensure that UAV can obtain ground image data stably, efficiently, and accurately.

In the acquisition of image data, multiple flights and multiple routes are required to ensure the overlap rate of image data [15]. The overlap rate includes course overlap rate and side overlap rate. The course overlap rate should be 60%~80%, and the minimum should not be less than 53%, according to the Regulations for Low-Altitude Digital Aerial Photography in China. The lateral overlap degree should be 15%~60%, and the minimum should not be less than 8%.

3.3.2. Ground Control Point and Checkpoint Coordinate Acquisition. Measuring points (control points and checkpoints) are the key data for constructing DSM and verifying the accuracy of the model. The Swiss Leica TS30 automatic total station and the Tianbao DiNi12 electronic level are adopted to measure points with accurate three-dimensional coordinates. The accuracy of the total station precision anomaly is 0.6 mm + 1 ppm, and the nominal accuracy of angle measurement is ±0.5". The nominal accuracy of the level is ±0.3 mm. According to the regulations of low-altitude digital aerial photogrammetry in China, the target image of the control point should be clear. It is easy to distinguish and measure the three-dimensional objects, such as the intersection point of fine linear ground objects with good angle (30°~150°), the obvious corner point of ground objects, and the point ground object center with no more than 3×3 pixels in the original image. At the same time, it

should be a place with small elevation fluctuation, relatively fixed all year round, and easy to accurately locate and measure. The intersection of linear features and hilltops should be suitable, while arc-shaped features, shadows, narrow gullies, sharp hilltops, and slopes with large elevation fluctuation should not be selected as the point targets. The point distance from the image edge should not be less than 150 pixels, other requirements remain unchanged.

3.4. Image Preprocessing

3.4.1. Distortion Correction. In addition to the mechanical and optical errors of the camera lens, the distortion difference may also come from the electrical errors during A/D conversion. The distortion difference destroys the parallel state of the outgoing ray and makes the image point deviate from the theoretical position, so it does not meet the condition of three-point collinearity. The camera distortion includes radial distortion and tangential distortion. The radial distortion comes from the shape of the lens, which is symmetric about the main optical axis of the camera. The object is imaged through this lens, and the farther the center of the lens is in the light, the more serious the image is bent [16]. The center distortion of imaging is defined as 0, and the distance between pixel point and image center (image origin) is

$$r = \sqrt{u^2 + v^2}. \tag{24}$$

The distortion is expanded by Taylor series near $r = 0$ position and described by the preceding terms, and the general expression is

$$f(r) = a_0 + a_1 r + a_2 r^2 \cdots. \tag{25}$$

When $r = 0$, the distortion is $f(r)0$, so $a_0 = 0$. And since the distortion function is radial symmetric with respect to r, the terms of odd power of r are all zero, so the radial distortion can be described as

$$\left. \begin{array}{l} \Delta x_r = u\left(k_1 r^2 + k_2 r^4 + k_3 r^6\right) \\ \Delta y_r = v\left(k_1 r^2 + k_2 r^4 + k_3 r^6\right) \end{array} \right\}, \tag{26}$$

where Δx_r and Δy_r are the offsets of radial distortion; k_1, k_2, and k_3 are radial distortion parameters.

Tangential distortion comes from the camera assembly process. Tangential distortion is caused by the fact that the lens and the image plane are not parallel when the sensor is installed on the camera. Tangential distortion offset can be expressed as

$$\left. \begin{aligned} \Delta x_t &= 2p_1 uv + p_2 \left(r^2 + 2x^2 \right) \\ \Delta y_t &= p_1 \left(r^2 + 2y^2 \right) + 2p_2 uv \end{aligned} \right\}, \tag{27}$$

where Δx_t and Δy_t are tangential distortion offset; p_1 and p_2 are tangential distortion parameters.

Camera distortion is the sum of radial distortion and tangential distortion, which can be expressed as

$$\left. \begin{aligned} \Delta x &= \Delta x_r + \Delta x_t \\ \Delta y &= \Delta y_r + \Delta y_t \end{aligned} \right\}. \tag{28}$$

The radial distortion parameters K1, K2, and k3 and tangential distortion parameters p1 and p2 can be obtained by calibrating the corner coordinates of the board, and then the image distortion can be corrected.

3.4.2. Uniform Color and Light. At present, almost all UAV images do not make full use of all the sensitive range of imaging sensors, and the latitude of all kinds of ground object target images is often limited to a relatively small range, which makes the images look not bright and clear. Many features and details obscure one another, making it difficult to identify. By uniformizing color and light, the dynamic variation range of image gray value can be enlarged, and the gray contrast between image elements can be increased, which is beneficial to improve the image quality.

In the case of underexposure or overexposure, the gray level of the image may be limited to a very small range. At this time, blurred images lacking gray level can be seen on the display [17]. In this study, linear transformation is used to linearly stretch the gray level of each pixel to achieve uniform color and light.

Assume that the grayscale range of the original image $f(i, j)$ is $[a, b]$, and the range of the image $g(i, j)$ after linear transformation is $[a', b']$, as shown in Figure 2. The relationship between $g(i, j)$ and $f(i, j)$ is shown as

$$g(i, j) = a' + \frac{b' - a'}{b - a} [f(i, j) - a] g(i, j) = a' + \frac{b' - a'}{b - a} [f(i, j) - a]. \tag{29}$$

3.4.3. MATLAB Programming

(1) Distortion Correction. According to the formula in 3.4.1, MATLAB is used to write programs to realize the automation and visualization of the image distortion correction process. The specific realization steps are as follows:
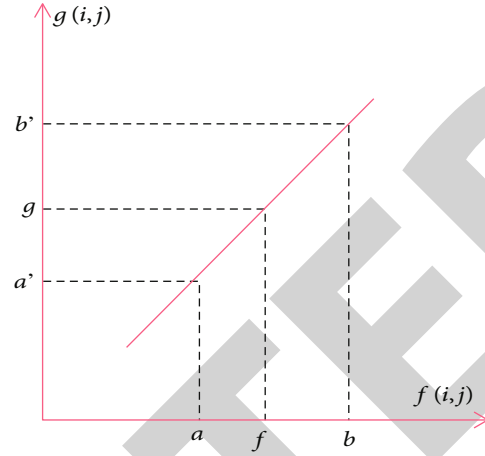

FIGURE 2: Gray value linear transformation.

(1) Run the main program of camera calibration and image preprocessing, and click "Distortion correction" on the page

(2) The program will call the calibration result file saved by the camera calibration before, and the prompt "Image Name:" will appear in the command window. Enter the name of the image to be corrected, for example, 20180520_00. Then the prompt "Image format:" appears in the command window. Enter the type of the image, such as JPG format, and enter "J"

(3) The program will correct the distortion of the image and name it "20180520_00_RECt" and save it to the original image path [18]. Outside the red boundary is the part with obvious changes

(2) Uniform Color and Light.

(1) Run the main program of camera calibration and image preprocessing. Click "Color and Light" on the page to enter the operation interface of color and light

(2) Enter the path of the image to be processed with uniform color and light in the "Input path of original Image" window, and enter the path of the image to be saved in the "Input Path of Saving" window

(3) Click "Start", and the program will read all the pictures under the original picture path through dir function; then the program uses stretchlim function to get the grayscale range [a,b] and uses imadjust function to linearly stretch the grayscale range of each pixel to [0,1]. At this point, we can observe the picture being processed in the right window of the main program interface, and the processing progress of the picture can also be observed in the command window. Finally, the program will save the processed image to the save path through imwrite function [19].

TABLE 2: Flight plan.

Parameters of the project	The values
Flight altitude per m	60
Course overlap rate/%	70
Lateral overlap rate/%	70
Shooting tilt angle/°	45
Flight sorties/sorties	5
Number of images of graduate school building	250
Number of images per piece of natatorium	122

TABLE 3: Coordinates of measuring points of graduate school building (unit: M).

Measuring point	X	Y	Z
P1	96861.49	45069.2211	43.5597
P2	96859.8948	45086.8363	41.3940
P3	96855.9084	45130.9944	33.5070
P4	96855.8831	45131.0000	43.5304
P5	96843.1660	45142.4365	34.8751
P6	96841.7762	45157.682	34.8544
P7	96840.4811	45172.6697	34.9033
P8	96849.1468	45152.3547	43.1990
P9	96858.2507	45104.9818	41.3740
P10	96839.8543	45179.6445	43.2833
P11	96838.4938	45194.8455	43.2784
P12	96831.4477	45196.0448	41.3622
P13	96835.8933	45223.4390	43.2436

TABLE 4: Coordinates of measuring points in the natatorium (unit: m).

Measuring point	X	Y	Z
P1	96847.89	45135.95	42.5805
P2	96845.92	45137.02	39.803
P3	96840.05	45140.19	39.808
P4	96834.47	45143.2	39.8047
P5	96828.97	45146.15	39.8227
P6	96823.4	45149.13	39.8123
P7	96817.79	45152.15	39.8209
P8	96812.23	45155.13	39.8153
P9	96806.71	45158.08	39.8201
P10	96801.19	45161.04	39.8198
P11	96795.68	45163.98	39.802
P12	96791.63	45162.3	39.802
P13	96782.89	45170.77	39.7922
P14	96780.85	45171.71	42.5439

3.5. Model Building. The process of model construction includes image area net joint adjustment, model surface reconstruction, and texture mapping. This study is mainly implemented by ContextCapture software. ContextCapture,
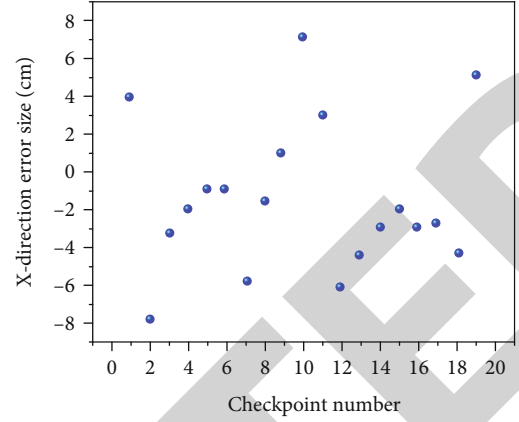

FIGURE 3: Error distribution in X direction of checkpoint.

a product of Acute3D, a French company Bentley acquired in 2015, quickly generates real-world models for various types of infrastructure projects.

3.5.1. Image Area Network Combined Adjustment. The joint adjustment of image area network is a key step in the process of model construction, which aims to obtain the external orientation elements and sparse 3D point clouds of all images. The combined adjustment method for the image area used by ContextCapture is as follows:

(1) Feature Detection. Firstly, the focal length information of the image is extracted. Then, scale-invariant feature transform (SIFT) algorithm is used to extract image features. SIFT is a descriptor with scale and rotation invariance, which has strong robustness and is suitable for extracting various image feature point information of scale transformation and rotation angle, with its accuracy. In the case that this offline algorithm does not need to consider the time cost, it also has advantages. SIFT algorithm calculates the location information of feature points through the Gaussian filter of different sizes (DOG).

(2) Feature Matching. The k-D Tree (K-Dtree) model is used to calculate Euclidean metric between feature points of two images to match feature points. K-Dtree can narrow the search scope and improve the matching efficiency [20]. When the feature points of each image are proposed, feature points are matched between pairs of images. Then for each image matching pair, its pole-opposite geometry is calculated. The fundamental matrix was estimated, and the matching pairs were optimized by Random Sample Consensus (RANSAC) algorithm. When all pairwise matching image pairs are determined, the common feature matching points that appear in multiple images can be connected to form a trajectory. Once all the corresponding trajectories are found, an image linkage graph can be constructed, which contains nodes of each image and edges of images with common trajectories.

(3) Aerial Triangulation by Light Beam Area Network. The aerial triangulation of light beam area network, also known
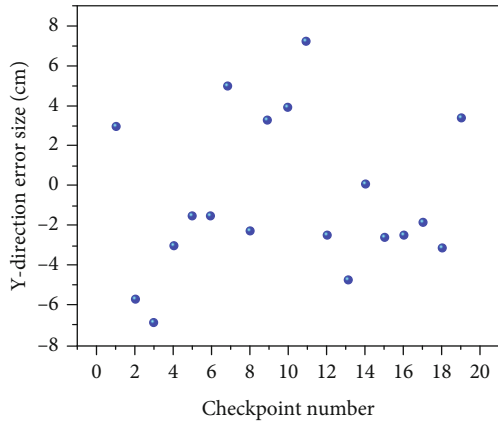
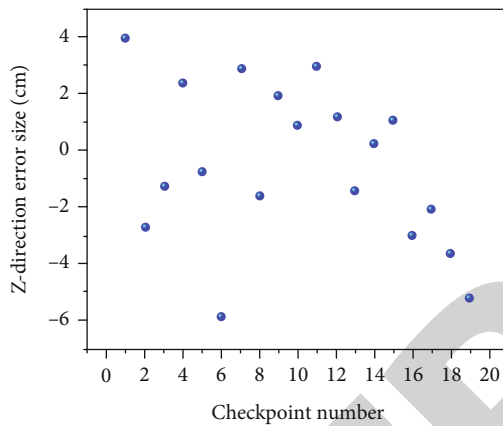Figure 4: Error distribution in Y direction of checkpoint.

Figure 5: Error distribution in Z direction of checkpoint.

Table 5: Test flight plan of an engineering.

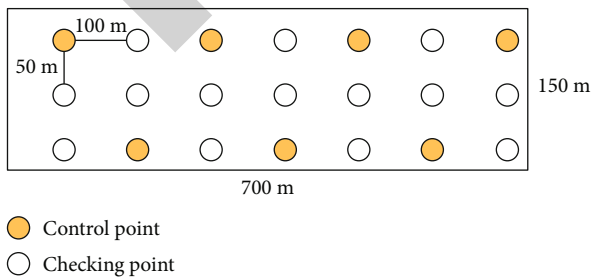| Parameters of the project	The values
Flight altitude per m	60
Course overlap rate/%	70
Lateral overlap rate/%	70
Shooting tilt angle/°	45
Flight sorties/sorties	5
Number of first images/piece	531
Number of second images/piece	505

Figure 6: Layout of an engineering test control point.

Table 6: Coordinates of measuring points of a project (unit: m).

Measuring point	X	Y	Z
P1	585620.518	3079090.949	6.322
P2	585590.168	3079043.052	6.446
P3	585567.408	3079007.109	6.391
P4	585542.057	3078967.163	6.480
P5	585516.672	3078927.115	6.524
P6	585488.859	3078883.081	6.362
P7	585463.459	3078843.084	6.320
P8	585632.279	3079085.404	1.952
P9	585604.905	3079039.434	1.801
P10	585576.645	3078999.235	2.086
P11	585550.369	3078960.674	2.258
P12	585526.347	3078920.353	2.151
P13	585497.812	3078879.218	2.163
P14	585472.573	3078839.281	2.181
P15	585655.945	3079067.893	0.960
P16	585628.257	3079024.092	0.944
P17	585602.537	3078983.366	0.953
P18	585576.898	3078942.889	1.002
P19	585551.214	3078902.388	1.009
P20	585525.475	3078861.956	0.938
P21	585499.728	3078821.151	0.875

as aerial triangulation of light beam area network, is based on a beam of light (image) composed of an image as the basic unit of adjustment. Based on the collinear equation of central projection as the basic equation of adjustment, a unified error equation and a French formula for the whole region were established to solve the three-dimensional coordinates of all points in the sparse three-dimensional point cloud and the six outer azimuth elements of each image in the region. The basic process is as follows: determine the external orientation elements and the 3D coordinate approximation of sparse point cloud; the error equation is established and normalized point by point. In the establishment of the reform formula, the modified equation is solved by the method and elimination cycle. Find out the outer square element of each image; the three-dimensional coordinates of sparse point cloud were calculated [21, 22].

3.5.2. Obtain Dense 3D Point Cloud. Only sparse discrete spatial points can be obtained through joint adjustment of image area network. However, in order to make reconstructed features smooth enough, dense matching between images is necessary to obtain dense three-dimensional point clouds. Dense matching and feature point matching have similarities, that is, they both seek point correspondence between multiple images, but they also have differences: first, dense matching requires much more computation and memory space than feature point matching. Therefore, solving the time and space complexity is the key of this kind of algorithm; secondly, the brightness variation near most pixels in the image is relatively small and does not have
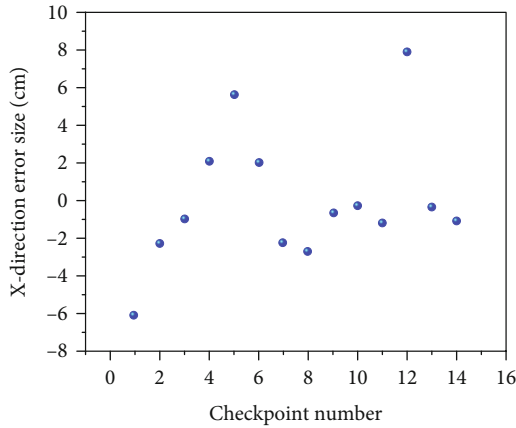
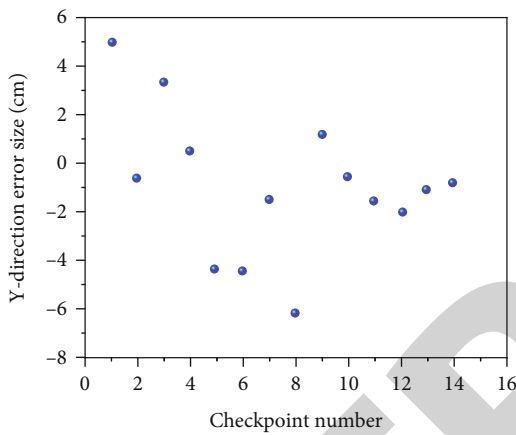Figure 7: Error distribution in X direction of checkpoint.

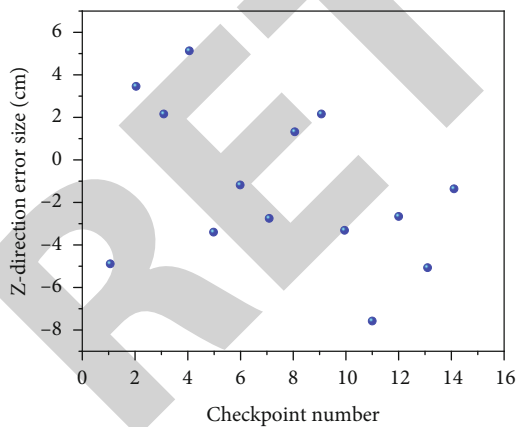Figure 8: Error distribution in Y direction of checkpoint.

Figure 9: Error distribution in Z direction of checkpoint.

the property of feature points, so dense matching generally requires more strict geometric constraints.

Density matching is based on geometric constraints and brightness correlation. The commonly used algorithm is adaptive matching method. The matching intensity of each matching point is calculated and sorted. If the matching intensity is high, the similarity between two points is high. Then there must be potential matching points around them,

and dense matching points can be found by setting certain Windows for matching diffusion [23]. After dense matching, the 3D coordinates of all pixels can be calculated by projection matrix or parallax. According to the above process, dense three-dimensional point cloud is finally obtained, which is the intermediate result of model construction.

3.5.3. Surface Mesh Reconstruction. Surface mesh reconstruction is to divide the region into connected triangular surface network according to the finite point set of the region and then achieve surface reconstruction. The shape and size of the triangular surface depend on the density and position of irregularly distributed measuring points, which can not only avoid data redundancy when the terrain is flat, but also represent digital elevation features according to terrain feature points [24]. At present, Delaunay triangulation is the most commonly used method for mesh reconstruction. It has a strong mathematical basis, and the triangular mesh is very uniform, which can accurately reconstruct the object surface.

The surface reconstruction process based on Delaunay triangulation is as follows: search the triangle or tetrahedron containing query points in dense point cloud; search the nearest neighbor points; query topological relationships or geometric attributes between neighboring points; add, delete, and move triangle vertices; constraints in the triangle subdivision boundaries; the polygon is triangulated and the triangle outside the region is deleted. The convex was calculated using Delaunay triangulation, and then the redundant tetrahedrons were gradually stripped away to make all data points visible, finally reconstructing the surface mesh model of the object.

3.5.4. Texture Mapping. Texture mapping is a necessary and key step to enhance the visual effect of the model. Texture mapping based on UAV tilt photogrammetry is multiview texture mapping, that is, multiple images from different viewpoints are used as texture maps.

The concrete implementation method of model texture mapping is as follows: obtaining surface 3D mesh data; the reference point of each triangle in the model is solved, that is, the best view of texture triangle; the texture coordinates of each surface triangle were solved, and the texture distribution was optimized iteratively by probability model. The boundary of the remaining texture after optimization is fused. For surface triangles in some areas, due to problems of shooting angle or occlusion, the corresponding texture triangles cannot be found in all input images and become surface cavities. Corresponding texture images need to be recollected for repair.

4. Results Analysis

4.1. 3D Model Construction of Buildings in a Campus. The objects of this model are the graduate school building and the natatorium. Among them, the graduate school building is a multistorey building with five floors (one underground and four above ground), with a total construction area of 29012.1 and a building height of 11.95 m. The natatorium

is a multistorey building with three floors (one underground and two above ground), with a total construction area of 6922.1 and a building height of 11.8 m.

The individuation of architecture is the development trend of today's architecture, and the appearance of architecture will be more and more diverse. The graduate school building and the natatorium have unique morphology and complex structure. If the traditional modeling method based on artificial ground image acquisition is adopted, it is difficult to obtain the workload and architectural detail texture, resulting in a large increase in rework probability. However, the modeling method based on UAV low-altitude aerial image is likely to be blocked by complex cutting and hollowing structures of buildings in some areas, resulting in the inability to obtain complete exterior surface texture of buildings [25]. Based on the above analysis, the 3D model construction of the graduate school building and the natatorium adopted the ultra-low-altitude aerial fine-model construction method based on UAV tilt photogrammetry. According to the rules of urban fine-3D model construction, the following flight plan was made (Table 2).

According to the point arrangement scheme of single building, four measuring points are selected as control points on the side of the building and the rest as checkpoints. Control points and checkpoints are obtained by Leica TS30 automatic total station, and their three-dimensional coordinates are shown in Tables 3 and 4.

To verify the 3D model accuracy of the graduate school building and the natatorium, error statistics were made for 19 checkpoints, and the statistical results are shown in Figures 3–5. The errors of the three directions are between -4 cm and 4 cm, accounting for 74%, and between -2 cm and 2 cm, accounting for 37%. The root mean square error of the three directions was calculated to be 4.0 cm, 3.8 cm, and 2.8 cm, respectively. It can be seen that the accuracy of single buildings obtained by this method is better than 4 cm, and the reliability is high, which meets the accuracy requirements of urban 3D model construction.

4.2. DSM Construction and Engineering Inspection of a Certain Project Reclamation Flood Dike. In order to verify the monitoring effect of UAV tilt photogrammetry technology on the reclamation of flood dike and other structures with large length, this study conducted on-site UAV inspection test. The test area is located in the southwest section of the seawall of the concrete mixing plant of a first-stage reclamation project. The length of the seawall in the aerial photography test is about 700 m.

According to the rule of DSM construction, the following flight plan (Table 5) was made, and the arrangement scheme of quantum-shaped control points was adopted in the test. As shown in Figure 6, coordinates of control points and checkpoints are obtained by RTK measurement, and their three-dimensional coordinates are shown in Table 6. There were two flight tests, 16 days apart, with identical flight plans. Clearly observed the changes in the DSM surface before and after construction. To verify the accuracy of DSM, error statistics were conducted for 14 checkpoints, and the statistical results are shown in Figures 7–9. The

errors of the three directions are between -4 cm and 4 cm, accounting for 74%, and between -2 cm and 2 cm, accounting for 50%. The root mean square error of the three directions was calculated as 2.3 cm, 2.5 cm, and 3.3 cm, respectively. It can be seen that the method not only has better precision than 4 cm, but also has high reliability.

5. Conclusion

Based on the 3D topography construction method based on UAV tilt photography-measurement, this essay builds a refined 3D model of the city and the best flight scheme and modeling scheme of DSM, which are applied to a campus complex and a project reclamation flood dike, and the following conclusions are drawn: Through the 3D model construction of a campus building complex, it can be seen that the precision of single buildings obtained by the ultra-low-altitude precision model construction method based on UAV tilt photogrammetry is better than 4 cm, and the reliability is high, which meets the precision requirements of urban real scene model construction. Through DSM construction and engineering inspection of a certain project reclamation flood dike, it can be known that a clear and high-precision digital surface model can be established based on UAV tilt photosurvey, which can meet the inspection and monitoring needs of reclamation flood dike and other oversized structures.

To sum up, it verifies the feasibility of the 3D topography construction method based on UAV tilt photogrammetry in practical engineering application and also verifies the reliability of the optimal flight scheme and modeling scheme for constructing urban fine 3D model and DSM. The 3D topography construction method based on UAV tilt photogrammetry can not only obtain high-precision 3D models of urban complex and single buildings, which can meet the requirements of digital city construction for 3D model construction, but also obtain clear and high-precision digital surface model. It can meet the inspection demand of super large structures such as flood dike and the monitoring demand of large deformation of sensitive points or postdisaster deformation.

Data Availability

The dataset can be accessed upon request.

Conflicts of Interest

The authors declare that they have no conflicts of interest.

Acknowledgments

References

[1] M. T. Mamaghani and Y. Hong, "Joint trajectory and power allocation design for secure artificial noise aided UAV communications," *IEEE Transactions on Vehicular Technology*, vol. 70, no. 3, pp. 2850–2855, 2021.

[2] K. Wang, C. Pan, H. Ren, W. Xu, L. Zhang, and A. Nallanathan, "Packet error probability and effective throughput for ultra-reliable and low-latency UAV communications," *IEEE Transactions on Communications*, vol. 69, no. 1, pp. 73–84, 2021.

[3] X. Luo, H. Long, S. Dong, and J. Wu, "Optimal surrender policy of guaranteed minimum maturity benefits in variable annuities with regime-switching volatility," *Mathematical Problems in Engineering*, vol. 2021, Article ID 9969937, 20 pages, 2021.

[4] M. Klanfar, T. Korman, D. Domitrovi, and V. Herceg, "Testing the novel method for angle of repose measurement based on area- weighted average slope of a triangular mesh," *Powder Technology*, vol. 387, no. 2, pp. 396–405, 2021.

[5] C. Wen, A. F. Habib, J. Li, C. K. Toth, and H. Fan, "Special issue on 3D sensing in intelligent transportation," *IEEE Transactions on Intelligent Transportation Systems*, vol. 22, no. 4, pp. 1947–1949, 2021.

[6] R. Alipour-Sarabi, Z. Nasiri-Gheidari, and H. Oraee, "Development of a three-dimensional magnetic equivalent circuit model for axial flux machines," *IEEE Transactions on Industrial Electronics*, vol. 67, no. 7, pp. 5758–5767, 2020.

[7] H. Sezer, J. H. Mason, I. B. Celik et al., "A transient three-dimensional mathematical model for the local impedance and polarization performance of planar SOFCs," *ECS Transactions*, vol. 103, no. 1, pp. 959–972, 2021.

[8] Y. Franco, M. Shani, G. Gat, and I. Shmulevich, "Three-dimensional dynamic model for off-road vehicles using discrete body dynamics," *Journal of Terramechanics*, vol. 91, no. 3, pp. 297–307, 2020.

[9] D. A. Chen, B. Rza, W. B. Lin, A. Sz, B. Xla, and C. Kd, "High energy density capacitors based on $0.88BaTiO_3$-$0.12Bi(Mg_{0.5}, Ti_{0.5})O_3/PbZrO_3$ multilayered thin films," *Ceramics International*, vol. 40, no. 4, pp. 5327–5332, 2014.

[10] W. Chen and J. Zhang, "Research on 3D modelling based on UAV tilt photogrammetry with KQCAM5 swing tilt camera," *Journal of Physics: Conference Series*, vol. 1650, no. 3, article 032156, 2020.

[11] J. Liu, "Application of UAV photogrammetry and 3D modeling in mine geological environment monitoring," *Acta Geologica Sinica*, vol. 93, no. z2, pp. 437-438, 2019.

[12] Y. Chen and J. Cao, "Research on quality inspection method of topographic map using oblique photogrammetry," *IOP Conference Series Earth and Environmental Science*, vol. 783, no. 1, article 012072, 2021.

[13] M. Li, D. Cheng, X. Yang et al., "High precision slope deformation monitoring by UAV with industrial photogrammetry," *IOP Conference Series: Earth and Environmental Science*, vol. 636, no. 1, 2021.

[14] I. Elkhrachy, "Accuracy assessment of low-cost unmanned aerial vehicle (UAV) photogrammetry," *Alexandria Engineering Journal*, vol. 60, no. 6, pp. 5579–5590, 2021.

[15] Z. Lv, Y. Wu, Q. Zhao, and X. M. Sun, "Design and control of a novel coaxial tilt-rotor UAV," *IEEE Transactions on Industrial Electronics*, vol. 69, no. 4, pp. 3810–3821, 2022.

[16] Z. Zhang, Z. Yuan, G. Ni, H. Lin, and Y. Lu, "The quality traceability system for prefabricated buildings using blockchain: an integrated framework," *Frontiers of Engineering Management*, vol. 7, no. 4, pp. 528–546, 2020.

[17] J. Liu and Z. Zou, "Application of BIM technology in prefabricated buildings," *IOP Conference Series: Earth and Environmental Science*, vol. 787, no. 1, 2021.

[18] W. Pan, K. Li, and Y. Teng, "Briefing: life-cycle carbon assessment of prefabricated buildings: challenges and solutions," *Proceedings of the Institution of Civil Engineers*, vol. 172, no. 1, pp. 3–8, 2019.

[19] H. Perez, J. Tah, and A. Mosavi, "Deep learning for detecting building defects using convolutional neural networks," *Sensors*, vol. 19, no. 16, p. 3556, 2019.

[20] A. Q. Bhatti and A. Wahab, "Analysis and design of emergency field isolation hospital building using innovative rapidly construction prefabricated units to treat patients infected with COVID-19," *Innovative Infrastructure Solutions*, vol. 6, no. 2, pp. 1–22, 2021.

[21] H. Xie, Y. Wang, Z. Gao, B. Ganthia, and C. Truong, "Research on frequency parameter detection of frequency shifted track circuit based on nonlinear algorithm," *Nonlinear Engineering*, vol. 10, no. 1, pp. 592–599, 2021.

[22] P. Ajay, B. Nagaraj, R. Arun Kumar, R. Huang, and P. Ananthi, "Unsupervised hyperspectral microscopic image segmentation using deep embedded clustering algorithm," *Scanning*, vol. 2022, Article ID 1200860, 9 pages, 2022.

[23] X. Liu, Y.-X. Su, S.-L. Dong, W.-Y. Deng, and B.-T. Zhao, "Experimental study on selective catalytic reduction of NO by C_3H_6 over Fe/Ti-PILC catalysts," *Ranliao Huaxue Xuebao/Journal of Fuel Chemistry and Technology*, vol. 46, no. 10, pp. 1231–1239, 2018.

[24] J. Jayakumar, B. Nagaraj, S. Chacko, and P. Ajay, "Conceptual implementation of artificial intelligent based E-mobility controller in smart city environment," *Wireless Communications and Mobile Computing*, vol. 2021, Article ID 5325116, 8 pages, 2021.

[25] N. Yuvaraj, K. Srihari, G. Dhiman, K. Somasundaram, and M. Masud, "Nature-inspired-based approach for automated cyberbullying classification on multimedia social networking," *Mathematical Problems in Engineering*, vol. 2021, Article ID 6644652, 12 pages, 2021.